Research Article | Vol. 10, No. 9 / 1 September 2019 / Biomedical Optics Express 4664
Biomedical Optics EXPRESS

Cell-to-cell influence on growth in large populations

MIKHAIL E. KANDEL,[1,2,6] WENLONG LU,[2,3,6] JON LIANG,[1] ONUR AYDIN,[4] TAHER A. SAIF,[4] AND GABRIEL POPESCU[1,2,5,*]

[1]Quantitative Light Imaging Laboratory, Department of Electrical and Computer Engineering, University of Illinois, Urbana, IL 61820, USA
[2]Beckman Institute, University of Illinois at Urbana-Champaign, Urbana, IL 61820, USA
[3]The State Key Laboratory of Digital Manufacturing Equipment and Technology, School of Mechanical Science and Engineering, Huazhong University of Science and Technology, Wuhan, China
[4]Department of Mechanical Science and Engineering, University of Illinois, Urbana, IL 61820, USA
[5]Department of Bioengineering, University of Illinois, Urbana, IL 61820, USA
[6]Denotes equal contribution
[*]gpopescu@illinois.edu

Abstract: Recent studies have revealed the importance of outlier cells in complex cellular systems. Quantifying heterogeneity in such systems may lead to a better understanding of organ engineering, microtumor growth, and disease models, as well as more precise drug design. We used the ability of quantitative phase imaging to perform long-term imaging of cell growth to estimate the "influence" of cellular clusters on their neighbors. We validated our approach by analyzing epithelial and fibroblast cultures imaged over the course of several days. Interestingly, we found that there is a significant number of cells characterized by a medium correlation between their growth rate and distance (modulus of the Pearson coefficient between 0.25-.5). Furthermore, we found a small percentage of cells exhibiting strong such correlations, which we label as "influencer" cellular clusters. Our approach might find important applications in studying dynamic phenomena, such as organogenesis and metastasis.

1. Introduction

Progress in systems biology has shown that emergent cellular phenomena such as differentiation and metastasis are driven by symmetry breaking [1]. Recent studies have revealed the importance of cellular *outliers*, which might be genetically programmed to disturb normal metabolism in a given system [2]. The development of 3D *ex vivo* tissue models for studying organ development, function, and disease face challenges when quantifying individual cell growth in highly heterogeneous systems [3–6]. It has been argued that, in developing *multicellular engineered living systems*, understanding emergence requires tremendous efforts not only in synthetic biology but also in characterization and imaging [7]. It is evident that assessing the behavior of individual cells in relation to the surrounding tissue is imperative.

Here, we investigate, for the first time to our knowledge, *spatial inhomogeneity* of cell growth rates in large populations, over several cell cycles. Understanding growth and homeostasis in mammalian cells has been described as "one of the last big unsolved problems" in cell biology [8]. Proliferation and differentiation are controlled by individual cells and cell populations in subtle ways that continue to elude scientists today [9–12]. From a clinical perspective, basic understating of cell growth kinetics and how it is modulated by disease and treatment will allow for more targeted drug development. Existing methods provide information on the overall effects of compounds on cell viability, but they are restricted to bulk measurements and require large sample sizes. One common approach is using the reduction of a colorless tetrazolium salt to yield a colored formazan, which is proportional to the number of viable cells. Although such

#367930 https://doi.org/10.1364/BOE.10.004664
Journal © 2019 Received 23 May 2019; revised 2 Aug 2019; accepted 6 Aug 2019; published 20 Aug 2019

Biomedical Optics EXPRESS

assays are useful for measuring the overall cytotoxic effectiveness of a compound, they lack the capability to measure proliferation kinetics at the individual cell level and to report on spatial inhomogeneities in the population [13].

Measuring the individual cell mass *vs.* growth rate, *M vs. dM/dt*, has the potential to reveal the mechanisms of coordination between cell cycle and cell growth [14,15] and determine whether the growth rate is proportional [16–18] or constant [9,19–21] with the cell mass. Linear growth would indicate that the rate of biosynthesis is dictated by the amount of DNA that can initiate the transcription process [10]. By contrast, the exponential growth model is based on the assumption that the cell mass production depends on the amount of ribosomal machinery and cytoplasm [10]. Thus, larger (heavier) cells produce more mass and accelerate in growth. In principle, linear growth can be maintained without a size-dependent mechanism, whereas the exponential growth requires a size-dependent mechanism to maintain homeostasis [16].

Performing direct mass measurements of individual live cells in cultures has been challenging for several reasons, including the cell's small size, morphological heterogeneity, adhesiveness, and wet environment [22]. Until recently, the state-of-the-art method to assess single cell growth rates over time was using Coulter counters to measure the volume of a large number of cells, in combination with careful mathematical analysis [23]. For relatively simple cells such as *Escherichia coli* (*E. coli*), traditional fluorescence microscopy techniques have also been used to assess growth in great detail [24]. In this type of method, the assumption is that volume is a good surrogate for mass; however, this assumption is not always valid, for example, due to variations in osmotic pressure [25]. Recently, shifts in the resonant frequency of vibrating microchannels have been used to quantify the buoyant mass of cells flowing through the structures [26,27]. Using this approach, Godin et al. have shown that several cell types grow exponentially, *i.e.*, heavier cells grow faster than lighter ones [27]. Later, the technology was upgraded to allow for parallel measurements of multiple cells [28]. While this method is sensitive enough to measure individual cell growth, it cannot be applied to adherent cell lines. To meet this challenge, this principle was extended to allow mass measurements on adherent cells by culturing cells directly on resonating pads [29]. This benefit comes at the expense of sensitivity and throughput.

Quantitative phase imaging (QPI) [30] is an interferometric, label-free approach that has found important applications in cell biology [31]. Cell growth has been one of the crucial applications of QPI, especially because the method is quantitative, lacks photobleaching, and presents low phototoxicity. The principle behind using interferometry to measure cell dry mass was established in the early 1950s when it was recognized that the optical phase delay accumulated through a live cell is linearly proportional to the dry mass (non-aqueous content) of the cell [32,33]. Since then, significant progress has been made using QPI to study cell mass and growth kinetics [25,34–39]. However, despite these advances, three main limitations commonly degrade the performance of quantitative phase imaging instruments: i) reduced contrast due to the speckle generated by the laser sources, ii) stability of the phase measurement, and iii) the complexity of experimental setups, which has presented practical obstacles for interoperability with existing workflows. An ideal method will perform parallel growth measurements on an ensemble of cells simultaneously and continuously over more than one cell cycle, quantify possible cell cycle phase-dependent growth, spatially-dependent growth, apply equally well to adherent and non-adherent cells, and integrate into existing workflows.

In order to study spatial correlations of growth rates in large populations of adherent cells, we used spatial light interference microscopy (SLIM) [40,41], which satisfies the constraints discussed above (Fig. 1(a). SLIM (*CellVista SLIM Pro*, Phi Optics, Inc.) is a highly sensitive quantitative phase instrument that combines white light illumination (thus, speckle-free) with common path interferometry (thus, highly stable) and can be implemented as an upgrade module onto existing phase contrast microscopes (thus, easy to adopt). The instrument is fully automated and capable of scanning large fields of view, such as multiwell plates. We applied SLIM to

Biomedical Optics EXPRESS

study growth in both fibroblasts (3T3) and epithelial (HeLa) cells. We found that both cell types grow exponentially and that the mass doubling times are heterogeneously distributed in space. The degree of correlation between the growth rates and spatial coordinate yields a quantitative descriptor for "cellular influence" that certain cells have on their neighbors. Remarkably, we discovered that, while most cells are not influential, a small portion of them appear to impose their growth rates over a large area around them. Finally, we found that the epithelial line contains a larger proportion of influential cells compared to the fibroblasts, which can be explained by their underlying function.

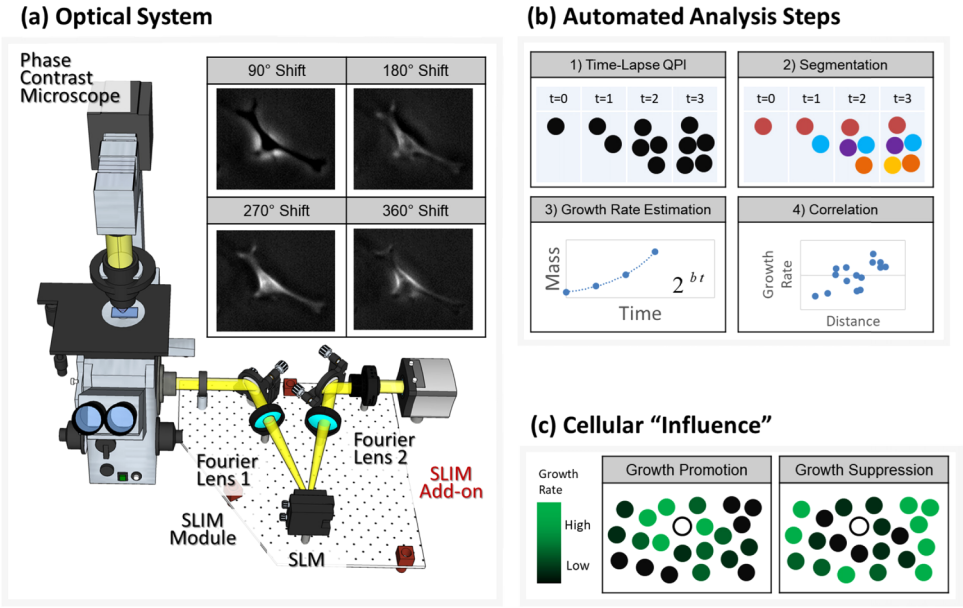

Fig. 1. Time-lapse quantitative phase imaging identifies influential cells by analyzing spatial variations in growth rates. **(a)** QPI images were acquired using SLIM (CellVista SLIM Pro, Phi Optics, Inc.). The SLIM module is attached to a commercial phase contrast microscope and introduces controlled phase-shifts with an SLM located at the position conjugate to the objective's back focal plane. Four such images are combined to form a phase map. **(b)** We acquire time-lapse QPI data that is then segmented into clusters. To estimate the influence of each cluster among its neighbors, we assign a growth rate to each cluster and analyze the correlation between growth rate and distance. Strong correlations hint that the cell may influence the growth of its neighbors. **(c)** "Influence" is understood as the ability of a cluster to promote or suppress the growth of its neighbors, so that cells that promote growth are likely to be surrounded by neighbors with higher growth rates.

2. Materials and methods

2.1. Microscopy

Schematic setup for SLIM (*CellVista SLIM Pro*, Phi Optics., Inc.) is shown in Fig. 1. The white light from a halogen lamp is projected onto a ring condenser aperture, which is used to illuminate the sample. At the back focal plane of the objective, a phase ring delays the incident light by a quarter wavelength with respect to the scattered light and also attenuates it to better match the intensities of the two interfering fields [42]. The image is delivered via the tube lens to the image plane, where the light is intercepted by the SLIM module (*CellVista SLIM Pro*, Phi Optics, Inc.). The Fourier lens L1 relays the back focal plane of the objective onto the surface of the

Biomedical Optics EXPRESS

spatial light modulator. Fourier lens L2 reconstructs the final image at the CCD plane, which is conjugated with the image plane. The lenses described were customized (Phi Optics, Inc.) to preserve diffraction limited resolution across the field of view. By displaying different masks on the SLM, the phase delay between the scattered and transmitted components is modulated in quadrature. The resulting four images are collated into a single image as outlined in [40].

2.2. Cell preparation

Fibroblasts (NIH/3T3, ATCC CRL-1658) and Epithelial (HeLa, ATCC CCL-2) cells were grown following vendor recommended procedure (ATCC). Before imaging, the cells were transferred to poly-d-lysine coated glass bottom Petri dishes (Cellvis). After allowing for six hours of attachment time, the cells were transferred to a thermally stabilized microscope with a mini-incubation chamber (AxioObserver Z1, Zeiss). To avoid focus drift due to thermal fluctuations, the cells were allowed to stabilize in the chamber for two hours before the start of imaging.

2.3. Cell segmentation procedure

To improve our segmentation performance, we analyzed the data as a three-dimensional stack with time as the third dimension. 3D morphological operations were performed using MATLAB on a computer with 256 Gb of RAM. The resulting process converts the time-lapse images of cells into "genealogical" trees, with cells splitting into branches after each division (Fig. 2).

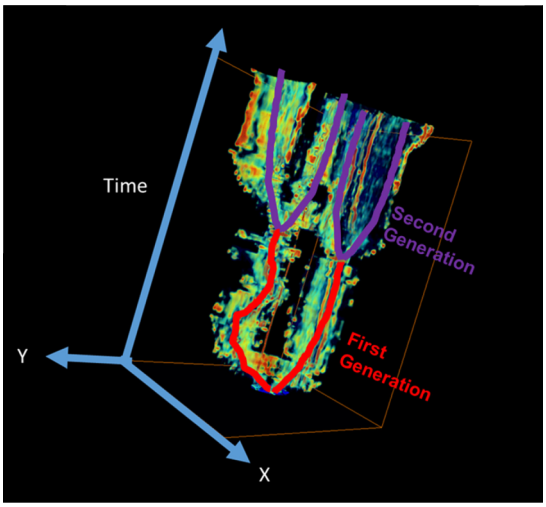

Fig. 2. Cell growth resembles a genealogical tree when time is taken as the 3rd dimension, with two daughter cells after the first division (red), and four daughter cells (purple) after the second division.

To generate the stack, we perform the following operations:

1) Phase data is pre-processed using a fast halo-removal algorithm [43]
2) 2D mosaic tiles are stitched into a single image (see section on Mosaic Generation)
3) Large 2D images are down-sampled to fit into computer memory and loaded as a 3D volume

Once the stack is ready, we perform segmentation according to the following recipe

4) A threshold is used to separate the cells from the background

Biomedical Optics EXPRESS

5) 3D dimensional hole filling refines the segmentation mask around the perimeter of the cell

6) A small 3D size threshold is used to remove debris

7) Cells that may have moved between time points are reconnected by applying dilation, followed by hole filling, and an erosion step to restore the original boundary

8) A temporal size filter removes cells that have detached (died) before the end of the experiment

9) 3D connected component analysis places a unique identifier on the remaining black and white clusters

2.4. Dry mass calculation and analysis

Following the procedure in [38], we recover the dry mass as

$$m(x,\ y) = \frac{\lambda}{2\pi\gamma}\phi(x,\ y) \tag{1}$$

where λ is the center wavelength; γ=0.2 ml/g is the refractive increment, and $\phi(x,\ y)$ is the measured phase.

2.5. Mosaic generation

The large fields of view used in this work were assembled from mosaic tiles aligned using software developed in-house [44]. In short, the algorithm estimates tile displacements with phase correlation. The global alignment error, due to disagreements between tile positions, is reduced in a least-squares fashion [45]. Following the implementation in [46] tiles are aligned through time, and the error tolerance for displacement estimation is decreased in an interactive fashion until the final configuration stabilizes.

2.6. Calculating the correlation coefficient between growth and distance

Our algorithm proceeds as follows: for the *i*th cluster's correlation coefficient, it finds all the nearby clusters within a distance R (400 μm in this work) away from the *i*th cluster giving a certain number of nearby clusters, *N*. This size scale, R, is selected by choosing the shortest distance that results in no qualitative changes in correlation coefficients. For example, at the limit of a very large size distance, the correlation coefficients tend to zero. Next, compute the distances between the j*t*h (j=1,2,. . . ,N) nearby cluster and the *i*th cluster by using the clusters' mass weighted centroids. In this experiment, we observe that the clusters do not migrate over time, and we use the centroid at the starting as the point from which distances are measured for subsequent time points. In such a way, for each cluster, it is possible to produce a scatter plot of growth rate and distance (Fig. 1(c)). From this plot, for each cluster, we compute the correlation coefficient between growth and distance, which is the *i*th cluster's correlation coefficient. The covariance between distance and growth rate is cov(r, b^{-1}), such that the Pearson correlation coefficient between growth and distance is,

$$\rho = \frac{\mathrm{cov}(r, b^{-1})}{\sqrt{\sigma_r \sigma_{b^{-1}}}} \tag{2}$$

Applying this algorithm to the whole field of view we can project the relative influence of each cluster on to the segmentation mask, arriving at a visual representation of cellular influence.

Biomedical Optics EXPRESS

3. Results

To determine influential cellular clusters, we monitored their growth rates relative to their neighbors (Fig. 1(b-c)). The SLIM instrument was used to scan large fields of view of live cells over several cell cycles (Fig. 1(b)). The goal is to generate a growth rate map of the cell population and quantify how it correlates with spatial distance. As shown in Fig. 1(b), we imaged and segmented the cells and compute the doubling times across the entire field of view. Then we calculated the Pearson correlation coefficient between the growth rate and distance from the center of the cluster. Finally, we generated a map of the correlation coefficients, which inform us on how similar growth of certain cell clusters is with respect to their surroundings. We refer to the clusters characterized by local minima or maxima in correlation coefficients as "influential" (Fig. 1(c)).

We performed time-lapse imaging of two different cell lines, HeLa (epithelial cells) and 3T3 (fibroblasts), questioning whether there is a qualitative difference between spatial correlations in cell growth in epithelial vs. fibroblast cells. Following the protocol described in Materials and Methods, we imaged 3T3 fibroblasts grown on poly-d-lysine coated Petri dishes. The field of view of the SLIM imaging was 16×16 mm^2 with a resolution of 1.07 μm (Fig. 2). The images were stitched from 11×13 mosaic tiles, to assemble the entire petri dish. The cells were monitored using the CellVista SLIM system over a period of 84 hours with a scan of the entire well performed every 30 minutes. A total of 157-time points was acquired. For accurate dry mass measurements, we applied the real-time halo removal algorithm, as described in Ref. [43].

Next, we converted the quantitative phase maps obtained by SLIM into cell dry mass density, as described in Materials and Methods. Figure 4 shows the dry mass density map associated with the 3T3 cell population, at the 42-hour mark, and different zoom levels. We developed an in-house algorithm for segmenting the cells into clusters. First, the dry-mass maps were binarized using a threshold to select all pixels slightly above zero mass. Next, the binary masks were filled to remove "holes" and objects smaller than a certain threshold were removed to eliminate the effects of debris (see Materials and Methods for details). The resulting masks were dilated with a disk structure element of radius 4 μm, followed by a second hole filling step. The resulting segmentation is shown in Fig. 4(b). We further refined our segmentation by including temporal information. With the understanding that cells are bound to the surface but debris and dead cells can detach, we used the following rules to segment clusters: 1) So long as a given cell group consists of more than a hundred pixels and exists in more than 154 (out of 157) images, we assume that the binary mask corresponds to a cellular cluster. 2) Any two different clusters should not overlap at any time. 3) The number of the clusters is expected to remain constant for the duration of the experiment. Using this procedure, we recorded 459 clusters for the experiment on the 3T3 culture presented in Figs. 2–5.

Once the cells were segmented, we plotted mass vs. time and confirmed that the growth curve is an exponential (Fig. 5). Thus, we assign a "growth rate" to each cluster, as defined by the mass doubling rate, b, from the fit with the exponential equation

$$m(t)/m_0 = 2^{bt} \tag{3}$$

In Eq. (1), $m(t)$ is the dry mass of the cluster at moment t, m_0 is the initial dry mass of the cluster, and b is the coefficient which represents the growth rate as an inverse doubling time (in h^{-1}). As discussed in [47], this exponential model is applicable when plating at low densities, before contact inhibition and other confluence related factors cause cell growth to plateau. As dying or otherwise disappearing clusters are removed during segmentation, we expect the growth rate to remain positive for the duration of the experiment. Therefore, we apply a "non-negative growth" prior. Specifically, we enforce the rule that the measured dry mass can never decrease and determine the growth rate from the adjusted curve (green), as shown in Fig. 5(b). Figure 5 shows a time-lapse sequence of a typical cluster with a growth coefficient of $b = 0.04\ h^{-1}$. This

Biomedical Optics EXPRESS

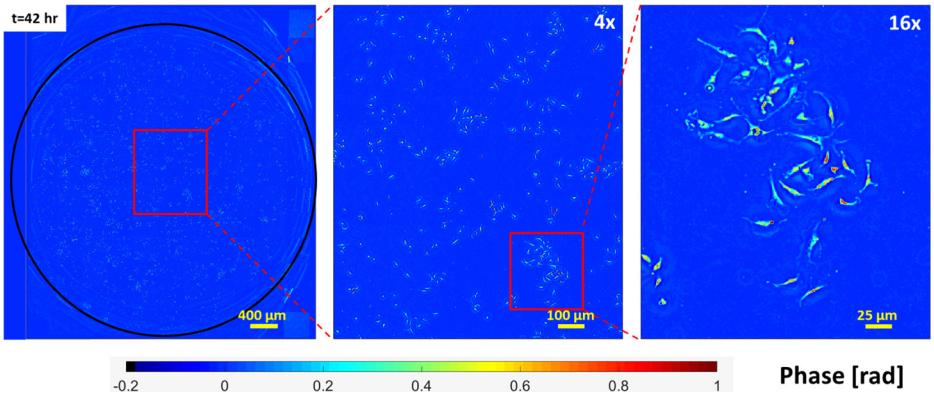

Fig. 3. Quantitative phase image of 3T3 fibroblasts. The phase map of the whole petri dish was reconstructed from mosaic tiles assembled by an in-house software. Data was acquired with a 5X/0.15NA objective.

(a) Dry Mass Calculation

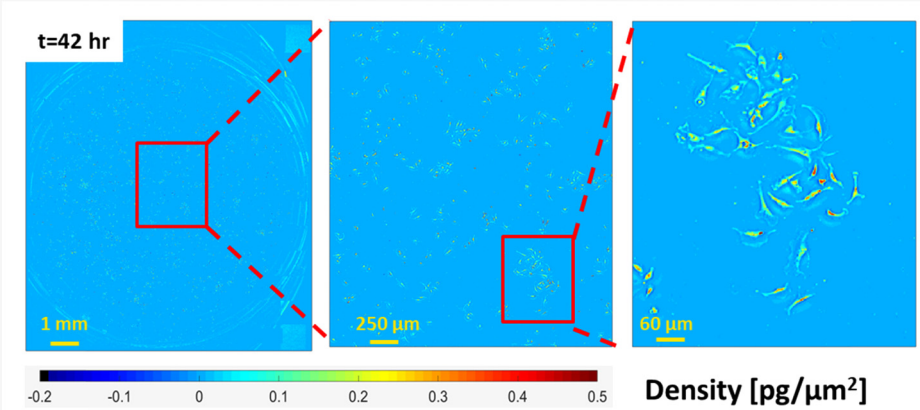

(b) Segmentation

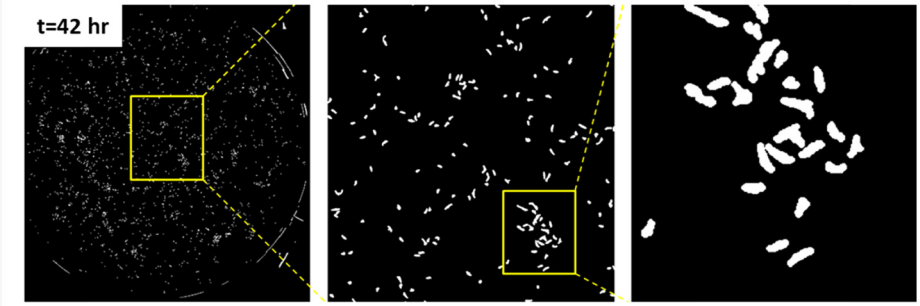

Fig. 4. Dry-mass and segmentation. (a) Cellular dry mass is proportional to the phase of halo-corrected slim images. A representative position of the sample at increasing zoom levels. **(b)** Segmentation is performed by a series of morphological operations as discussed in Results.

Biomedical Optics EXPRESS

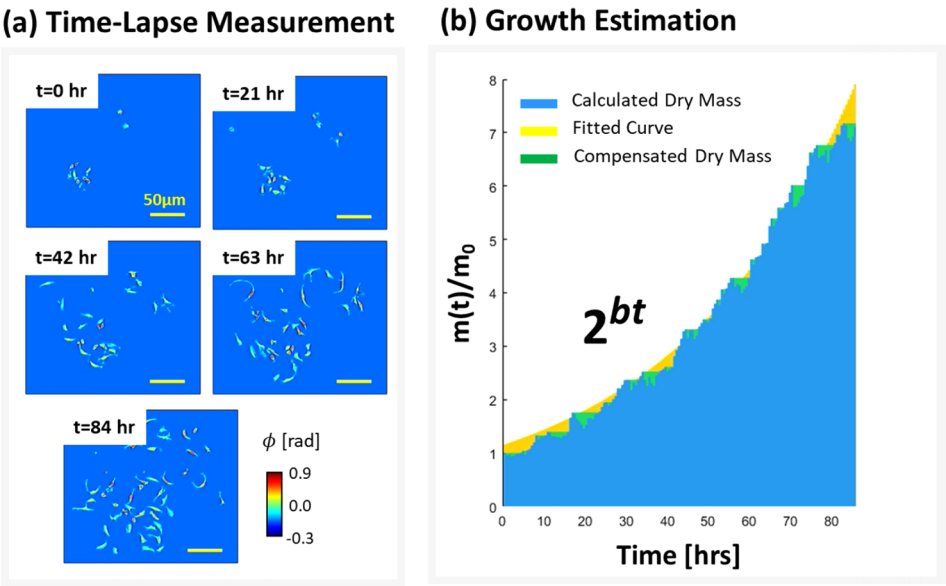

Fig. 5. Estimation of dry mass doubling time from time-lapse SLIM images. **(a)** Phase maps of a single cluster at the times indicated. **(b)** Relative dry mass change vs. time for a given cluster normalized by the first time point (Calculated Dry Mass). To account for phase-wrapping in dividing cells, we compensate the dry mass so that the total never decreases over time. The final doubling time coefficient is estimated form this compensated curve.

b-value corresponds to a 25 hour doubling time, which is in good agreement with the expected cell count doubling times for 3T3 cells [48]. However, we do not expect the mass and count to double at the same rate, as the mass per cell may vary with time (see, e.g., Ref. [36]).

Figure 6 shows the growth coefficients, *b*, for each cluster projected onto the segmentation map at the start, middle (t = 43 h), and end of the experiment. In this experiment, the distribution of cell mass doubling coefficients (*b*) indicates that most clusters have a growth rate of $0.03\ h^{-1}$, which implies most of the clusters will double in mass within 33 hours.

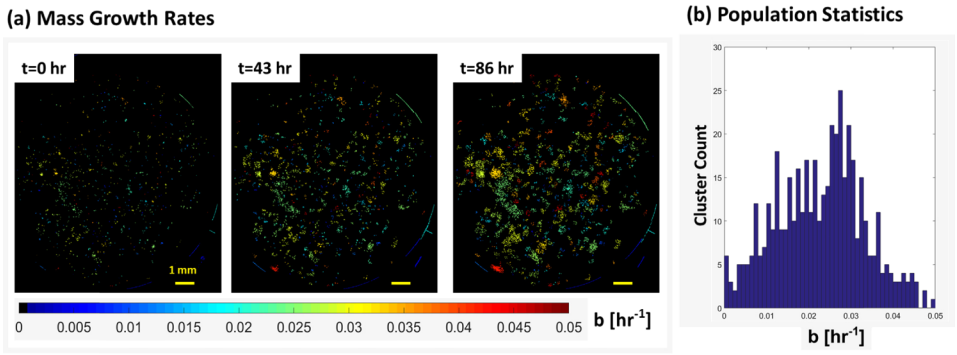

Fig. 6. Timelapse cell growth with projected growth rates. **(a)** Calculated growth coefficient, b, is projected onto the black and white segmentation to produce a time-lapse sequence showing the spatial distribution of cellular growth. **(b)** Histogram of growth coefficients.

Biomedical Optics EXPRESS

To visualize the relative influence of clusters on their neighbors, we determine the correlation between the growth rate, b, and the distance from the cluster center, r. This analysis is the main result of the work. The hypothesis behind this approach is that cells will promote or suppress the growth of their neighbors, leading to a relationship between the growth of the cluster's neighbors and the distance from the cluster. If the Pearson correlation coefficient of b and r is negative, the cluster can be understood as suppressing the growth of its neighborhoods, as moving towards the cluster results in decreasing growth. If the correlation coefficient of a cluster is positive, cells

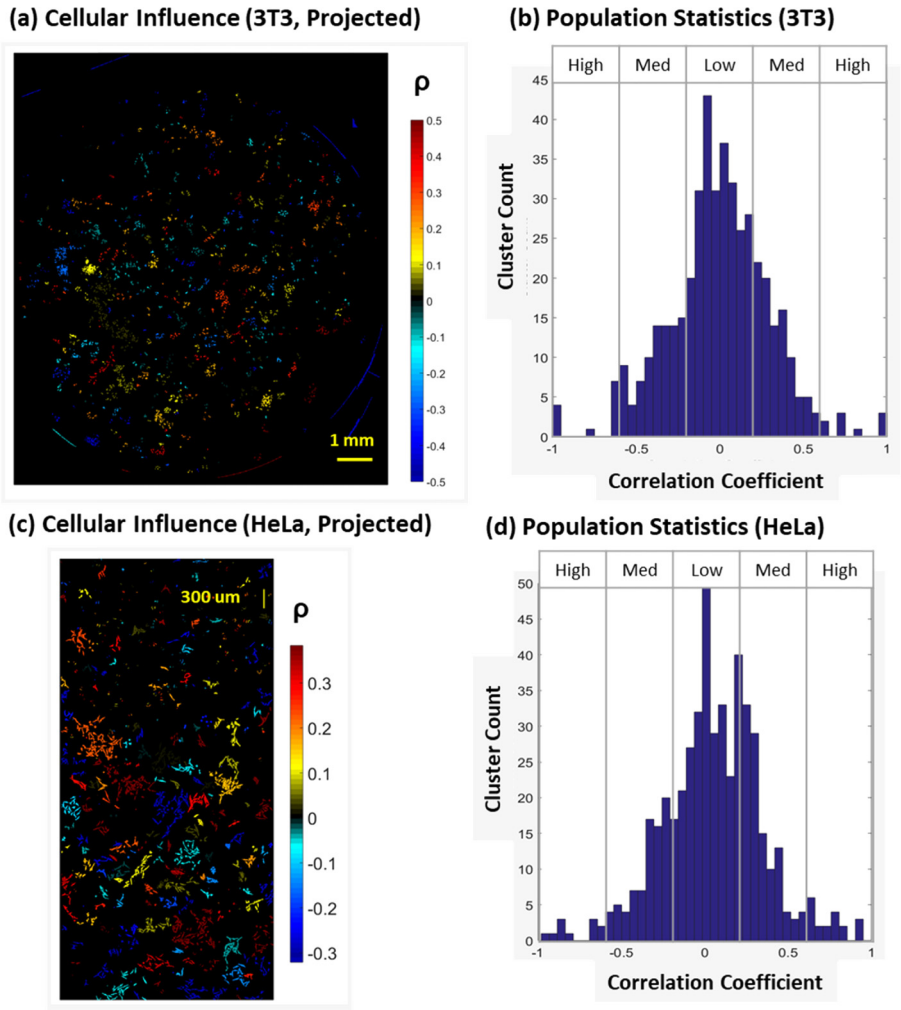

Fig. 7. Projection of cellular influence (see also Visualization 1, Visualization 2, and Visualization 3). **(a)** Correlation coefficients for the 3T3 culture are projected onto the segmentation map at the end of the experiment. This gives a spatial distribution of correlation coefficients. **(b)** Histogram of the correlation coefficient for all 3T3 clusters. **(c)** Correlation coefficients for the HeLa culture are projected onto the segmentation map at the end of the experiment. **(d)** Histogram of the correlation coefficient for all HeLa clusters. **(e)** When comparing the population statistics, as a percentage of the population described by the influence value, it is apparent that 3T3 cells composed of a population with weakly coupled (low p) clusters, while HeLa cells have a larger tail distribution indicating more, highly coupled clusters.

Biomedical Optics EXPRESS

nearer to the cluster have higher growth rates, hinting that the cluster is promoting growth. When no strong relationship exists, the cell cluster is not "influential".

We performed the same analysis on a commonly used line of epithelial cells (HeLa cells). The results of are shown in Visualization 1, Visualization 2, and Visualization 3, showing the phase map, growth rates, and projection of the magnitude influence. The distribution of the correlation coefficients for all clusters is shown in Fig. 7(b, d). From Fig. 7, we can see that while most clusters do not have substantial influence over their neighbors ($|\rho|<0.3$), several clusters exhibit substantial correlation coefficients (Fig. 7(a), red) marking them as cells of interest. A typical cluster has approximately 20 neighbors, which for a $\rho = 0.5$ implies a 0.95 confidence interval of [0.04,0.78] [49].

4. Discussion

In this work, we presented a quantitative analysis to determine influential cells from time-lapse measurements of cellular dry mass. Due to the high quality of the SLIM images, we can use low-magnification objectives, enabling us to rapidly digitize large areas with reduced photo-toxicity. From these data, we can directly measure the mass of individual cells over an entire petri dish through several cell cycles. Furthermore, as phase maps are interferometrically normalized, the processing is straightforward with adequate results achieved using simple morphological operations. Note that such studies on large populations of adherent cells are impossible to perform using vibrating cantilever techniques. Previous reports showed that fibroblasts respond to signals from epithelial cells [50]. Studying the co-culture of epithelial cells and fibroblasts are the subject of current investigation.

Funding

National Science Foundation (CBET-0939511 STC, NRT-UtB 1735252); National Institute of General Medical Sciences (GM129709).

Acknowledgments

MK proposed the experiment and performed imaging. MK and WL performed analysis. MK, WL, GP wrote the manuscript. Cells were provided by JL, OA, and TS. GP supervised the project.

Disclosures

GP has a financial interest in Phi Optics Inc, a company developing quantitative phase imaging instruments.

References

1. J. J. Frost, K. J. Pienta, and D. S. Coffey, "Symmetry and symmetry breaking in cancer: a foundational approach to the cancer problem," OncoTargets Ther. **9**(14), 11429–11440 (2018).
2. R. J. DeBerardinis and C. B. Thompson, "Cellular Metabolism and Disease: What Do Metabolic Outliers Teach Us?" Cell **148**(6), 1132–1144 (2012).
3. J. W. Brown and J. C. Mills, "Implantable synthetic organoid matrices for intestinal regeneration," Nat. Cell Biol. **19**(11), 1307–1308 (2017).
4. N. Gjorevski and M. P. Lutolf, "Synthesis and characterization of well-defined hydrogel matrices and their application to intestinal stem cell and organoid culture," Nat. Protoc. **12**(11), 2263–2274 (2017).
5. V. Munnamalai and D. M. Fekete, "Building the human inner ear in an organoid," Nat. Biotechnol. **35**(6), 518–520 (2017).
6. N. de Souza, "Stem cells: Organoid variability examined," Nat. Methods **14**(7), 655 (2017).
7. R. D. Kamm, R. Bashir, N. Arora, R. D. Dar, M. U. Gillette, L. G. Griffith, M. L. Kemp, K. Kinlaw, M. Levin, and A. C. Martin, "Perspective: The promise of multi-cellular engineered living systems," APL Bioeng. **2**(4), 040901 (2018).
8. J. B. Weitzman, "Growing without a size checkpoint," J. Biol. **2**(1), 3 (2003).

Biomedical Optics EXPRESS

9. M. Brackstone, J. L. Townson, and A. F. Chambers, "Tumour dormancy in breast cancer: an update," Breast Cancer Res. **9**(3), 208 (2007).
10. A. F. Chambers, A. C. Groom, and I. C. MacDonald, "Dissemination and growth of cancer cells in metastatic sites," Nat. Rev. Cancer **2**(8), 563–572 (2002).
11. P. Goss, A. L. Allan, D. I. Rodenhiser, P. J. Foster, and A. F. Chambers, "New clinical and experimental approaches for studying tumor dormancy: does tumor dormancy offer a therapeutic target?" APMIS **116**(7-8), 552–568 (2008).
12. K. W. Hunter, N. P. Crawford, and J. Alsarraj, "Mechanisms of metastasis," Breast Cancer Res. **10**(S1), S2 (2008).
13. B. A. Teicher, D. L. Selwood, and P. A. Andrews, "Anticancer drug development: preclinical screening, clinical trials and approval (vol 91, pg 1000, 2004)," Br. J. Cancer **91**(11), 1977 (2004).
14. R. A. Weinberg, "The many faces of tumor dormancy," APMIS **116**(7-8), 548–551 (2008).
15. H. Wikman, R. Vessella, and K. Pantel, "Cancer micrometastasis and tumour dormancy," APMIS **116**(7-8), 754–770 (2008).
16. M. D. Cameron, E. E. Schmidt, N. Kerkvliet, K. V. Nadkarni, V. L. Morris, A. C. Groom, A. F. Chambers, and I. C. MacDonald, "Temporal progression of metastasis in lung: cell survival, dormancy, and location dependence of metastatic inefficiency," Cancer Res **60**, 2541–2546 (2000).
17. A. K. Croker and A. L. Allan, "Cancer stem cells: implications for the progression and treatment of metastatic disease," J. Cell. Mol. Med. **12**(2), 374–390 (2008).
18. K. Pantel and R. H. Brakenhoff, "Dissecting the metastatic cascade," Nat. Rev. Cancer **4**(6), 448–456 (2004).
19. P. Hahnfeldt, D. Panigrahy, J. Folkman, and L. Hlatky, "Tumor development under angiogenic signaling: a dynamical theory of tumor growth, treatment response, and postvascular dormancy," Cancer Res **59**, 4770–4775 (1999).
20. I. C. MacDonald, A. C. Groom, and A. F. Chambers, "Cancer spread and micrometastasis development: quantitative approaches for in vivo models," BioEssays **24**(10), 885–893 (2002).
21. G. N. Naumov, I. C. MacDonald, P. M. Weinmeister, N. Kerkvliet, K. V. Nadkarni, S. M. Wilson, V. L. Morris, A. C. Groom, and A. F. Chambers, "Persistence of solitary mammary carcinoma cells in a secondary site: a possible contributor to dormancy," Cancer Res **62**, 2162–2168 (2002).
22. G. Popescu, K. Park, M. Mir, and R. Bashir, "New technologies for measuring single cell mass," Lab Chip **14**(4), 646–652 (2014).
23. A. Tzur, R. Kafri, V. S. LeBleu, G. Lahav, and M. W. Kirschner, "Cell growth and size homeostasis in proliferating animal cells," Science **325**(5937), 167–171 (2009).
24. G. Reshes, S. Vanounou, I. Fishov, and M. Feingold, "Cell shape dynamics in Escherichia coli," Biophys. J. **94**(1), 251–264 (2008).
25. G. Popescu, Y. Park, N. Lue, C. Best-Popescu, L. Deflores, R. R. Dasari, M. S. Feld, and K. Badizadegan, "Optical imaging of cell mass and growth dynamics," Am. J. Physiol. Cell Physiol. **295**(2), C538–C544 (2008).
26. A. K. Bryan, A. Goranov, A. Amon, and S. R. Manalis, "Measurement of mass, density, and volume during the cell cycle of yeast," Proc. Natl. Acad. Sci. U. S. A. **107**(3), 999–1004 (2010).
27. M. Godin, F. F. Delgado, S. Son, W. H. Grover, A. K. Bryan, A. Tzur, P. Jorgensen, K. Payer, A. D. Grossman, M. W. Kirschner, and S. R. Manalis, "Using buoyant mass to measure the growth of single cells," Nat. Methods **7**(5), 387–390 (2010).
28. N. Cermak, S. Olcum, F. F. Delgado, S. C. Wasserman, K. R. Payer, M. A. Murakami, M. Knudsen, R. J. Kimmerling, M. M. Stevens, Y. Kikuchi, A. Sandikci, M. Ogawa, V. Agache, F. Baleras, D. M. Weinstock, and S. R. Manalis, "High-throughput measurement of single-cell growth rates using serial microfluidic mass sensor arrays," Nat. Biotechnol. **34**(10), 1052–1059 (2016).
29. K. Park, L. Millet, J. Huan, N. Kim, G. Popescu, N. Aluru, K. J. Hsia, and R. Bashir, "Measurement of Adherent Cell Mass and Growth," Proc. Natl. Acad. Sci. U. S. A. **107**(48), 20691–20696 (2010).
30. G. Popescu, *Quantitative Phase Imaging of Cells and Tissues*, McGraw-Hill Biophotonics (McGraw-Hill, 2011).
31. Y. Park, C. Depeursinge, and G. Popescu, "Quantitative phase imaging in biomedicine," Nat. Photonics **12**(10), 578–589 (2018).
32. R. Barer, ""Phase-contrast" methods and birefringence," Nature **167**(4251), 642–643 (1951).
33. H. G. Davies and M. H. Wilkins, "Interference microscopy and mass determination," Nature **169**(4300), 541 (1952).
34. G. A. Dunn and D. Zicha, "Dynamics Of Fibroblast Spreading," J. Cell Sci. **108**, 1239–1249 (1995).
35. K. Lee, K. Kim, J. Jung, J. Heo, S. Cho, S. Lee, G. Chang, Y. Jo, H. Park, and Y. Park, "Quantitative phase imaging techniques for the study of cell pathophysiology: from principles to applications," Sensors **13**(4), 4170–4191 (2013).
36. M. Mir, A. Bergamaschi, B. S. Katzenellenbogen, and G. Popescu, "Highly Sensitive Quantitative Imaging for Monitoring Single Cancer Cell Growth Kinetics and Drug Response," PLoS One **9**(2), e89000 (2014).
37. S. Sridharan Weaver, Y. Li, L. Foucard, H. Majeed, B. Bhaduri, A. J. Levine, K. A. Kilian, and G. Popescu, "Simultaneous cell traction and growth measurements using light," J. Biophotonics **12**(3), e201800182 (2019).
38. M. Mir, Z. Wang, Z. Shen, M. Bednarz, R. Bashir, I. Golding, S. G. Prasanth, and G. Popescu, "Optical measurement of cycle-dependent cell growth," Proc. Natl. Acad. Sci. U. S. A. **108**(32), 13124–13129 (2011).
39. M. Mugnano, P. Memmolo, L. Miccio, S. Grilli, F. Merola, A. Calabuig, A. Bramanti, E. Mazzon, and P. Ferraro, "In vitro cytotoxicity evaluation of cadmium by label-free holographic microscopy," J. Biophotonics **11**(12), e201800099 (2018).
40. Z. Wang, L. J. Millet, M. Mir, H. Ding, S. Unarunotai, J. A. Rogers, M. U. Gillette, and G. Popescu, "Spatial light interference microscopy (SLIM)," Opt. Express **19**(2), 1016 (2011).

Biomedical Optics EXPRESS

41. T. Kim, R. J. Zhou, M. Mir, S. D. Babacan, P. S. Carney, L. L. Goddard, and G. Popescu, "White-light diffraction tomography of unlabeled live cells," Nat. Photonics **8**(3), 256–263 (2014).
42. Z. Wang, I. S. Chun, X. L. Li, Z. Y. Ong, E. Pop, L. Millet, M. Gillette, and G. Popescu, "Topography and refractometry of nanostructures using spatial light interference microscopy," Opt. Lett. **35**(2), 208–210 (2010).
43. M. E. Kandel, M. Fanous, C. Best-Popescu, and G. Popescu, "Real-time halo correction in phase contrast imaging," Biomed. Opt. Express **9**(2), 623–635 (2018).
44. M. E. Kandel, S. Sridharan, J. Liang, Z. Luo, K. Han, V. Macias, A. Shah, R. Patel, K. Tangella, A. Kajdacsy-Balla, G. Guzman, and G. Popescu, "Label-free tissue scanner for colorectal cancer screening," J. Biomed. Opt. **22**(6), 066016 (2017).
45. B. S. Reddy and B. N. Chatterji, "An FFT-based technique for translation, rotation, and scale-invariant image registration," IEEE Trans. Image Process **5**(8), 1266–1271 (1996).
46. G. Quadrato, T. Nguyen, E. Z. Macosko, J. L. Sherwood, S. Min Yang, D. R. Berger, N. Maria, J. Scholvin, M. Goldman, J. P. Kinney, E. S. Boyden, J. W. Lichtman, Z. M. Williams, S. A. McCarroll, and P. Arlotta, "Cell diversity and network dynamics in photosensitive human brain organoids," Nature **545**(7652), 48–53 (2017).
47. ATCC, "Passage Number and Population Doubling Level," *ATCC Animal Cell Culture Guide*, p. 4.
48. S. T. Christensen, I. R. Veland, A. Schwab, M. Cammer, and P. Satir, "Chapter Three - Analysis of Primary Cilia in Directional Cell Migration in Fibroblasts," in *Methods in Enzymology*, W. F. Marshall, ed. (Academic Press, 2013), pp. 45–58.
49. R. Lowry, "The Confidence Interval of rho", retrieved http://vassarstats.net/rho.html.
50. J. P. Thiery, H. Acloque, R. Y. Huang, and M. A. Nieto, "Epithelial-mesenchymal transitions in development and disease," Cell **139**(5), 871–890 (2009).